Phase-stable and selectable repetition-rate division of an optical frequency comb

Tariq Shamim Khwaja[1] and Tai Hyun Yoon[1,2,*]
[1]Department of Physics, Korea University, Seoul 02841, Republic of Korea
[2]Center for Molecular Spectroscopy and Dynamics, Institute for Basic Science (IBS), Seoul 02841, Republic of Korea

(Received 30 June 2020; accepted 29 September 2020; published 19 October 2020)

We present a phase-stable and selectable repetition-rate ($f_{\rm rep}$) divider (PSRD) of an optical frequency comb (OFC) by down-picking a train of pulses from the fundamental OFC phase coherently. The PSRD operating at the integer pulse-picking order p uses an acousto-optic modulator driven by a train of phase-synchronized single-cycle wave packets oscillating at the carrier frequency of $f_c \equiv f_{\rm rep}$ and the gating frequency of $f_g^p \equiv f_{\rm rep}/p$. The demonstrated PSRD can selectively pick a train of pulses with $p = 2$ to 25 from the fundamental OFC with $f_{\rm rep} = 250$ MHz at 530 nm. Integrated phase noises from 10 Hz to 25 kHz offset frequency from the optical beat note between each down-picked OFC and the fundamental OFC are measured to be about (59 ± 6) mrad through the whole pulse picking order. The phase-coherent down-picked OFC could be of use for various applications where phase-stable and repetition-rate selectable OFCs are the essential radiation sources.

DOI: 10.1103/PhysRevA.102.043515

I. INTRODUCTION

Optical frequency comb (OFC) [1–3], a precise ruler in the frequency and time domains, has expedited many breakthroughs in precision measurement science such as timekeeping [4], high-resolution spectroscopy [5], molecular fingerprinting [6], and dimensional metrology [7,8] to name a few. Recently, the use of frequency combs in quantum technology has also gained attractions where quantum OFC exhibits multimode entangled photon states and thus shows great promises for further developments of quantum information processing technology [9–16], quantum metrology [17], quantum spectroscopy [18,19], and imaging [20] with undetected photons. Depending on the specific application of the quantum OFC, the emergent quantum technology requires different kinds of radiation sources of quantum-correlated signal-idler photon pairs that has discrete spectral and temporal modes [12,16,21–24]. They can be generated, for example, by using spontaneous parametric down-conversion (SPDC) processes from a nonlinear crystal [12] or an atomic ensemble [25–27], four-wave mixing from an optical fiber [28] and microring resonator [11,29], and stimulated (or seeded) parametric down-conversion (StPDC) processes [30–33].

In particular, in the parameter regime of unresolved spectral and temporal modes of the quantum OFC, a frequency comb single-photon interferometry [33] and an interferometric spectroscopy with undetected photons [19] have been demonstrated without heralded generation and detection of signal and idler photons. In these demonstrations, two independent but identical single-photon frequency combs, an optical frequency comb consisting of single-photons per pulse, are generated from two StPDC crystals pumped by the same OFCs and simultaneously injection seeded by the same highly coherent continuous-wave idler fields. Here the quantum coherence between two independent but identical single-photon frequency combs is induced quantum optically by making the photon statistics of two single-photon-added coherent states of the conjugated idler photons indistinguishable without overlapping two idler paths, which is in sharp contrast to the concept of induced coherence by the laser proposed by the Mandel group in 1990 [30–32], where the idler photon paths must be overlapped for path indistinguishability. More recently, based on these techniques of the frequency comb single-photon interferometry and spectroscopy with undetected photons, a novel rovibrational spectroscopy for real molecular gases that has high frequency resolution and remote measurement capabilities with undetected photons has been reported [34].

In both demonstrations in Refs. [19,33], however, single-photon detection per each signal pulse (time bin) of the single-photon frequency comb was not possible due to the 4-ns-long pulse-to-pulse time interval (PPTI) of the generated single photons at the signal wavelength, since the repetition rate ($f_{\rm rep} = 250$ MHz) of the OFC used for the pump source of two StPDC crystals is too fast compared to the counting rate of the state-of-the-art single-photon detector. The PPTI of 4 ns is indeed about 15 times shorter compared to the typical dark period ($\sim$60 ns) of the single-photon avalanche photodiode (SAPD) [35,36]. Thus, for the time-bin-resolved single-photon detection, the pulse-to-pulse temporal separation of the single-photon frequency comb must exceed the dead time of the SAPD.

Toward this way, a phase-stable operation of a pulse picker by using an acousto-optic modulator (AOM) has been demonstrated [37,38] with an OFC from the Ti:sapphire laser to seed an optical fiber amplifier. In Ref. [37] a synchronicity condition is proposed and demonstrated by choosing the AOM carrier frequency (f_c) as the integer ratio of $f_{\rm rep}$, i.e., $f_c = (u/p) f_{\rm rep}$,

---

[*] thyoon@korea.ac.kr

where u and p are integers, to maintain the phase and amplitude stability of the down-picked OFC constant. In this paper we demonstrate a phase-stable and selectable repetition-rate divider (PSRD) of an OFC by synchronous picking a train of pulses from the fundamental OFC down to the PPTI of 100 ns ($f_{\mathrm{rep}} = 10$ MHz), which is much longer than the dead time of the SAPD, with zero carrier-envelop phase. We envision that the present work opens a way for future experiments based on the time-bin resolved single-photon detection of the single-photon frequency comb with equal pulse-to-pulse phase slip.

II. PHASE-STABLE AND SELECTABLE REPETITION-RATE DIVIDER

In the present paper we used an AOM as a pulse picker whose driving signal of frequency f_c is not only phase synchronized to the f_{rep} of the fundamental OFC [37], but also fully amplitude modulated, i.e., it is a single-cycle wave packet (SCWP) with a selectable gating frequency of $f_g^p = f_{\mathrm{rep}}/p$. Figure 1(a) illustrates the schematic diagram of the proposed phase-stable repetition-rate divider (PSRD). The fundamental OFC at 530 nm with a pulse width of 10 ps and the spectral width of 2 ns is generated by the frequency doubling (SHG) of an amplified Yb fiber OFC around 1060 nm (FC1000-250-WG, Menlo Systems). The repetition frequency f_{rep} and the carrier-envelop offset frequency f_{ceo} of the fundamental OFC are phase locked to be $f_{\mathrm{rep}} = 250$ MHz and $f_{\mathrm{ceo}} = 20$ MHz, respectively, with reference to the reference signals from the GPS disciplined Rb atomic clock. We used the same OFC for the experiments of the frequency comb single-photon interferometry and the high-resolution spectroscopy with undetected photons in the previous publications [19,33]. As explained earlier, in Refs. [19,33], a single-photon frequency comb at the signal wavelength was generated from the StPDC crystal pumped by the fundamental OFC, where the PPTI of 4 ns of the generated single-photon frequency comb is too short compared to the dark period of 60 ns of the SAPD. Thus, it was not possible to detect single photon per each time bin of 4 ns in the previous experiments. Instead, in [19,33], the time-averaged single-photon count for 10 ms was measured by using a single-photon sensitive electron multiplying charge-coupled device (EMCCD) to measure the single-photon interference fringes. To study the single-photon statistics, however, such as $g^2(\tau)$ and coincident count to evaluate the purity of the generated single-photon states, there remains a technical challenge to make the single-photon generation rate slower than the dark period of the SAPD. This is the main subject of the present study.

The optical frequency of the nth mode of the fundamental OFC in the middle panel of Fig. 1(b) can be written as $f_n = nf_{\mathrm{rep}} + f_{\mathrm{ceo}}$. In order to divide the repetition rate of the fundamental OFC phase coherently with an integer division (picking) order p from $f_{\mathrm{rep}}^p = 125$ MHz ($p = 2$) down to 10 MHz ($p = 25$), we design a single-cycle wave packet (SCWP) as shown in the upper panel of Fig. 1(b) to drive the traveling-wave AOM (MT250-A0.5-VIS, AA Opto-Electronic) as a phase-coherent pulse picker. To minimize the phase noise contribution introduced by the PSRD in Fig. 1, the synchronicity condition of the driving frequency of the AOM proposed in [37] is implemented. By adjusting the pulse width of the gating RF signal to be exactly same as the oscillation period of 4 ns of the carrier wave, we are able to generate phase-synchronized SCWP with tunable gating frequency. Experimentally, a RF signal at 250 MHz from the frequency synthesizer (8664A, Agilent) and a 4-ns-long gating pulse from the pulse generator (8131A, Hewlett-Packard) are mixed by the DBM to generate the phase-locked SCWP as shown in Fig. 1(a). Here the time bases of the pulse generator and the frequency synthesizer are phase locked to the same reference signals of 10 MHz from the Rb clock. Finally, the train of SCWPs is amplified up to 1 W to drive the AOM with a carrier frequency of $f_c = f_{\mathrm{rep}} = 250$ MHz and the gating frequency of $f_g^p = f_{\mathrm{rep}}/p$, satisfying the synchronicity condition of Eqs. (2) and (3).

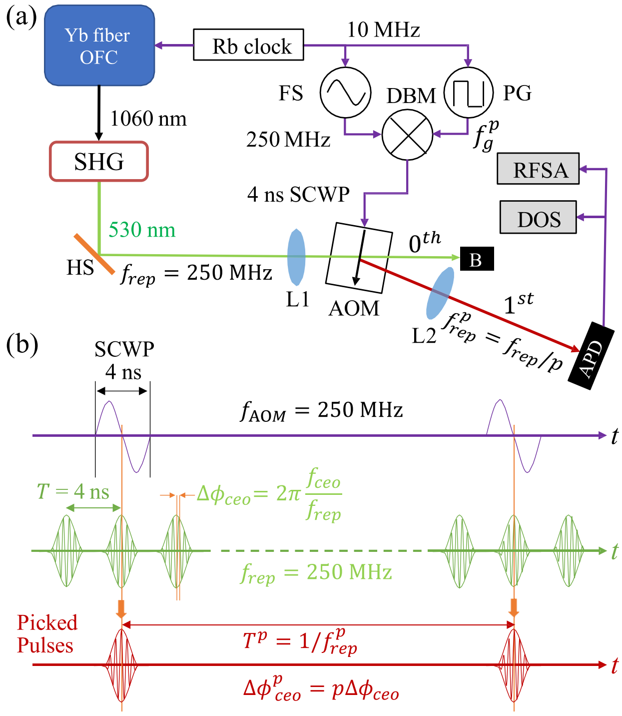

FIG. 1. (a) Schematic diagram of the PSRD. The fundamental OFC at 530 nm with a pulse width of 10 ps is generated from an Yb fiber OFC at 1060 nm. Single-cycle wave packet (SCWP) with an oscillation period of 4 ns to drive the traveling-wave AOM is generated by mixing a continuous-wave RF signal with a carrier frequency of $f_c = 250$ MHz and a 4-ns-long square gating pulse by the DBM. (b) Upper panel: RF signal of the SCWP with $f_c = f_{\mathrm{rep}}$ of the fundamental OFC. The desired integer picking order p of the PRRD determines the frequency of the square gating pulse, of which period is given by $T^p = 1/f_g^p = p/f_{\mathrm{rep}}$. Middle panel: A pulse train with the PPTI of $T = 4$ ns of the fundamental OFC with $f_{\mathrm{rep}} = 250$ MHz and $f_{\mathrm{ceo}} = 20$ MHz. The carrier-envelop phase of the fundamental OFC is given by $\Delta\phi_{\mathrm{ceo}} = 2\pi f_{\mathrm{ceo}}/f_{\mathrm{rep}}$. Lower panel: Down-picked OFC with a repetition rate of $f_{\mathrm{rep}}^p = f_{\mathrm{rep}}/p$ and carrier-envelop phase slip of $\Delta\phi_{\mathrm{ceo}}^p = p\Delta\phi_{\mathrm{ceo}}$. SHG: second harmonic generation, HS: harmonic separator, FS: frequency synthesizer, PG: pulse generator, DBM: double-balanced mixer, B: beam block, L1, L2: focusing and collimating lens, APD: avalanche photodiode, RFSA: radio-frequency spectrum analyzer, DOS: digital oscilloscope.

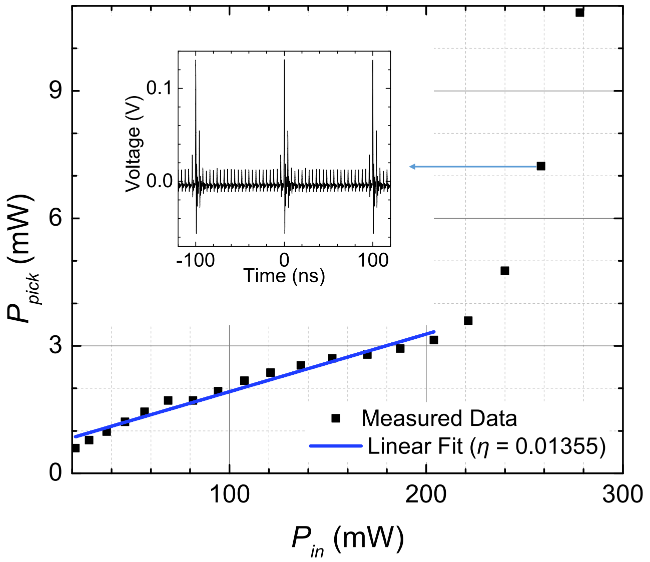

FIG. 2. Output power $P_{\rm pick}$ of the down-picked OFC for $p = 25$, where $f^p_{\rm rep} = 10$ MHz and $f^p_{\rm ceo} = 0$, versus input power $P_{\rm in}$ of the fundamental OFC with $f_{\rm rep} = 250$ MHz. Statistical uncertainties for 20 measurements per each point are smaller than the data symbols. The straight line with the slope $\eta = 0.014$ is the linear fit to the data in the nonspatial overlapping regime (see main text). Inset shows the time trace of the pulse train of the down-picked OFC for at $P_{\rm in} = 258$ mW, which clearly shows the spatial overlap between the zeroth- and first-order diffracted beams at the detector (see small peaks with 4 ns time intervals between major peaks with 100 ns time intervals).

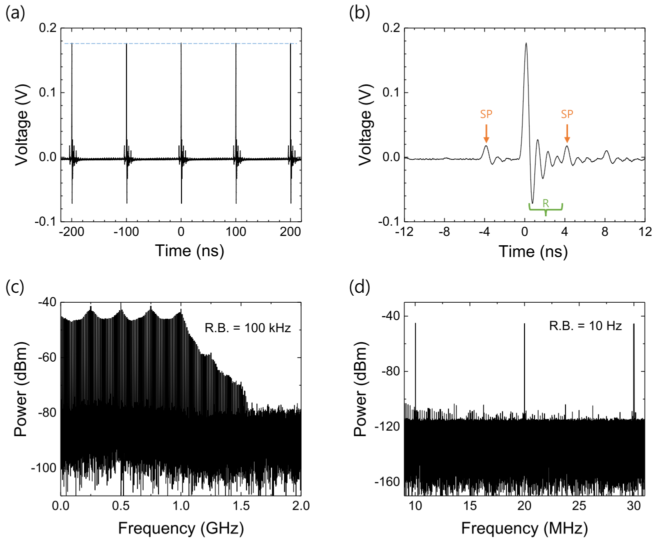

FIG. 3. (a) A train of pulses of the down-picked OFC for $p = 25$ with $f^p_{\rm rep} = 10$ MHz and $f_{\rm ceo} = 0$ and the expanded view (b) of a single picked pulse. Due to the finite speed of the acoustic wave in the AOM, there are nonzero side peaks (SPs) 4 ns apart, those are the undesired adjacent pulses diffracted during the SCWP transit across the focused beam at the AOM (see Appendix). The damped ringing signal (R) is caused by the finite bandwidth of 1 GHz of the APD. (c) Power spectrum of (a) recorded by the RF spectrum analyzer with the resolution bandwidth of 100 kHz, and its expanded view (d) showing three harmonics of $f^p_{\rm rep} = 10$ MHz of the down-picked OFC with the resolution bandwidth of 10 Hz. Nonzero side peaks in (b) are manifested as 250 MHz periodic spectral modulation of the RF trace in (c). The signal to noise ratios (SNRs) in (d) are over 70 dB and small peaks with SNRs below 10 dB are electrical noise spikes.

Then, the optical frequency of the down-picked OFC in the positive first-order diffracted beam, as shown in the lower panel of Fig. 1(b), is Doppler shifted by the carrier frequency of the AOM so that the optical frequency of the mth mode of the down-picked OFC may be written as

$$f^p_m = m f^p_{\rm rep} + f^p_{\rm ceo}, \tag{1}$$

where m is an integer, and the repetition-rate $f^p_{\rm rep}$ and the carrier-envelope phase slip $\Delta\phi^p_{\rm ceo}$ of the down-picked OFC are, respectively, given by

$$f^p_{\rm rep} = \frac{f_{\rm rep}}{p}, \tag{2}$$

$$\Delta\phi^p_{\rm ceo} = 2\pi\frac{p}{a}, \bmod 2\pi, \tag{3}$$

where $a = f_{\rm rep}/f_{\rm ceo} = 12.5$. Note here that for $p = 25$, $f^p_{\rm rep} = 10$ MHz and $f^p_{\rm ceo} = 0$ Hz so that the down-picked OFC becomes a train of pulses having $T^p = 100$ ns, which is larger than the dead time of 60 ns of the SAPD, as well as having the zero carrier-envelop phase slip, opening a possibility to generate a single-photon pulse train with zero phase slips for the frequency comb single-photon interferometry with high visibility [33].

III. EXPERIMENTAL RESULTS

Experimental results for $p = 25$, which is the highest pulse picking order achieved in the present work, i.e., lowest repetition rate of $f^p_{\rm rep} = 10$ MHz, are shown in Figs. 2 and 3. We study the $p = 25$ case extensively, because it is the pulse train with $f^p_{\rm ceo} = 0$ as well as $T^p = 100$ ns, which is longer than the typical dead time of the SAPD of 60 ns [35,36].

Figure 2 shows the down-picked output power $P_{\rm pick}$ of the down-picked OFC versus input power $P_{\rm in}$ of the fundamental OFC with $f_{\rm rep} = 250$ MHz. Up to $P_{\rm in} \lesssim 204$ mW, i.e., $P_{\rm pick} \lesssim 3.1$ mW, $P_{\rm pick}$ increases linearly as $P_{\rm in}$ increases, but for $P_{\rm in} > 205$ mW, there is a sharp rise in $P_{\rm pick}$ due to the spatial overlap between the zeroth- and first-order diffracted beams at the detector. When the fundamental OFC is focused tightly on the AOM to get a high diffraction efficiency, the complete separation between the first-order diffracted beam from the undiffracted zeroth-order beam becomes impractical due to the trade-off relation between the divergence angle of the Gaussian beam and the Bragg angle of the diffracted beam depending on the beam waist. At the fixed beam waist on the AOM, the physical separation between them at the position of the collimation lens is inversely proportional to the input power due to the increase of the effective Gaussian beam diameter at higher beam intensity (see Appendix). In the nonspatial overlapped regime, $P_{\rm pick}$ increases linearly as $P_{\rm pick} = \eta P_{\rm in}$ (blue line), where $\eta = \xi/p \sim 0.014$ and $\xi \sim 0.34$ is the diffraction efficiency. Statistical uncertainties for 20 measurements per each point in Fig. 2 are smaller than the size of each data symbol, indicating unidentified systematic effect is introduced in the linear regime. Inset in Fig. 2 shows the time trace of the pulse train of the down-picked OFC at $P_{\mathrm{in}} = 258$ mW, which clearly shows the spatial overlap between the zeroth- and first-order diffracted beams at the detector (see small peaks with 4 ns time intervals between major peaks of 100 ns time intervals). Note here that, in the nonspatial overlapping regime, it is possible to separate the first-order beam from the zeroth-order one so that there is no interference seen in the inset of Fig. 2 as demonstrated in Fig. 3.

Figure 3 shows the details of the temporal measurement and the spectral measurements of the down-picked OFC for $p = 25$ at $P_{\mathrm{pick}} = 3.1$ mW. Here the experimental parameters are chosen after considering the trade-off relation of the temporal and spatial overlap issues of the PSRD as described in Appendix. The time trace of the pulse train with $T = 100$ ns in Fig. 3(a) and its expanded view in Fig. 3(b) detected by the fast digital oscilloscope (DOS) in Fig. 1 clearly demonstrate the performance of our PSRD with high pulse-picking efficiency. As can be seen in Fig. 3, there is no spatial overlap observed in the inset of Fig. 2 at high input power for $P_{\mathrm{in}} > 258$ mW. Instead, we observed symmetric side peaks due to the temporal overlap of the adjacent pulses with the 4-ns-long SCWP as it transits across the Gaussian beam waist of $w_0 = 12.6$ μm at the AOM.

Minimizing the spatial overlap to effectively isolate the down-picked OFC out of the undiffracted fundamental OFC and the temporal overlap to reduce the side peak powers are subject to the trade-off condition between the transit time $\Delta\tau$ of the SCWP across the beam waist at the AOM and the divergence angle θ_{div} of the Gaussian beam at the AOM, both depend on the beam waist w_0, as described in Appendix.

After taking into account the trade-off relation for the spatial and temporal overlapping issues, we obtained the data in Fig. 3, where the timing of the gating signal of the SCWP to drive the AOM of the PSRD was adjusted such that the side peaks have equal amplitudes. The power ratio of the side peaks relative to the main peak of the down-picked OFC is about 16% with the optical parameters given in Appendix. The damped ringing signal (R) after the main pulse is caused by the finite bandwidth of 1 GHz of the APD. We note that the time-domain traces also show no significant amplitude fluctuations as the synchronicity condition given in Eqs. (2) and (3) are strictly maintained experimentally by stabilizing f_{rep} and f_{ceo} of the fundamental OFC as well as the SCWP by employing the phase-locking loops.

The RF spectra in Figs. 3(c) and 3(d) measured by the RFSA in Fig. 1 show equidistant comb teeth with a spacing of 10 MHz as expected from the comb spacing division of 250 MHz by the pulse picking order of $p = 25$. The resolution bandwidth in Figs. 3(c) and 3(d) are 100 kHz and 10 Hz, respectively. Imperfect side peak suppression also manifests itself as periodic spectral modulation with 5 dB magnitude and 250 MHz spectral period as seen in Fig. 3(c). Decrease of the spectral power beyond 1 GHz frequency is due to the bandwidth limit of the APD. The signal-to-noise ratio (SNR) of the beat notes at 10 MHz and its harmonics in Fig. 3(d) is more than 70 dB, which is similar to that of ~80 dB of the fundamental OFC. Small peaks in Fig. 3(d) with the SNR of less than 10 dB are electronic noises. In order to fully access the properties of the down-picked OFC at different pulse picking order p, the phase noise characteristics are evaluated as discussed in the following section.

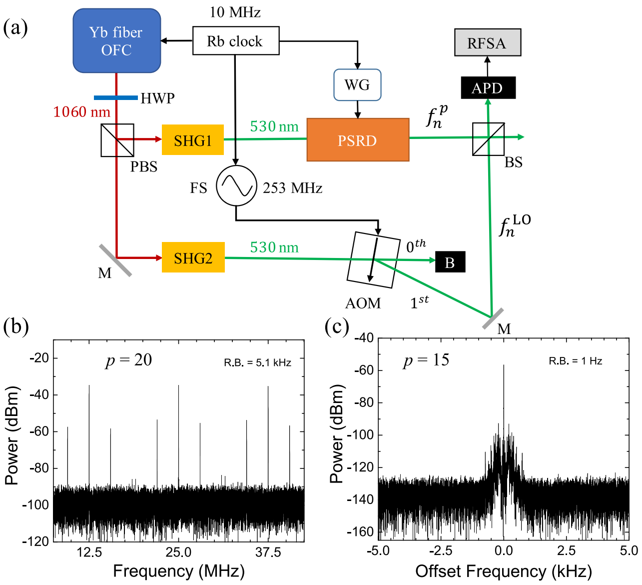

FIG. 4. (a) Experimental setup to measure the phase noise of the down-picked OFC with reference to the independent source of fundamental OFC as the local oscillator (LO). The optical frequencies of the reference LO are shifted by +253 MHz by an acousto-optic frequency shifter. To select the pulse picking order p from $p = 1$ to $p = 25$, we used a waveform generator to trigger the electrical gating pulse of the pulse generator in Fig. 1. (b) A typical beat note spectrum between the LO and the down-picked OFC for $p = 20$, where $f_{\mathrm{rep}}^{p} = 12.5$ MHz with the resolution bandwidth of 5.1 kHz. (c) Double-side power spectral density of the beat note at the carrier frequency of 47 MHz for $p = 15$ with the resolution bandwidth of 1 Hz, which has integrated phase noise of 51.6 mrad from 10 Hz to 25 kHz (see Fig. 5).

IV. PHASE NOISE MEASUREMENTS

To evaluate the phase noise characteristics of the PSRD, a heterodyne beat detection setup between the down-picked OFC and the reference fundamental OFC with $f_{\mathrm{rep}} = 250$ MHz as the local oscillator (LO) is implemented as illustrated in Fig. 4(a). Here PSRD is the same setup described in Fig. 1(a), except the pulse generator is now triggered by the tunable reference wave from a waveform generator (Moku:Lab, Liquid Instruments) by varying the frequency from 125 MHz for $p = 2$ to 10 MHz for $p = 25$. Note here that any phase noise associated with the radiation source can be canceled out efficiently because it has two identical sources of fundamental OFC at two different paths for the PSRD and the LO.

In Fig. 4 the optical frequency of the LO is shifted by 253+ MHz, thus the optical frequency of the nth mode may be written as $f_n^{\mathrm{LO}} = (n+1)f_{\mathrm{rep}} + f_{\mathrm{ceo}} + 3$ MHz. After the LO is combined spatially with the output of the down-picked OFC by the BS and temporally by adjusting the path-length difference between two paths to be equal, the LO is superposed by the down-picked OFC at the APD to generate beat notes

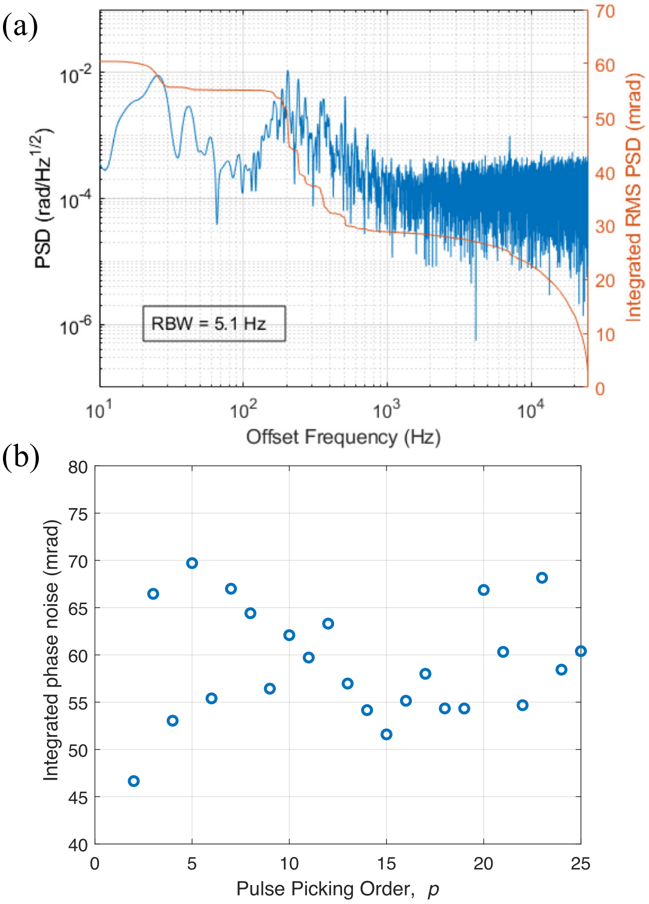

FIG. 5. (a) Single-sided power spectral density (PSD) with the resolution bandwidth of 5.1 Hz (left vertical axis, blue line) as a function of offset frequency from 10 Hz to 25 kHz at the carrier frequency of 27 MHz for $p = 25$. Integrated phase noise from 10 Hz to 25 kHz (right vertical axis, red line) is also shown. (b) Integrated phase noise versus pulse picking order p from $p = 2$ to $p = 25$. Here the mean value and standard deviation of the integrated phase noise are 59 and 6 mrad, respectively.

between them. The optical frequency of the down-picked OFC with a pulse picking order p is given by $f_m^p = m f_{\rm rep}^p + f_{\rm ceo}^p$, where $f_{\rm rep}^p$ and $f_{\rm ceo}^p$ are given in Eqs. (2) and (3), respectively, resulting in the beat notes at $|f_n^{\rm LO} - f_m^p| = m f_{\rm rep}^p \pm 3$ MHz. As an example, Fig. 4(b) shows the typical beat note spectrum measured by the RFSA with the RB of 5.1 kHz for $p = 20$. Here the peaks at $n f_{\rm rep}^p = 12.5$, 25, and 37.5 MHz for $n = 1$, 2, and 3, respectively, are the harmonics of the $f_{\rm rep}$ of the down-picked OFC itself as expected, while peaks at $n f_{\rm rep}^p \pm 3$ MHz are the beat notes between the fundamental OFC and down-picked OFC. Figure 4(c) shows the extended view of the two-sided power-spectral density of the beat note at 47 MHz, i.e., $3 f_{\rm rep}^p - 3$ MHz for $p = 15$, with the RB of 1 Hz, which has the integrated phase noise of 51.6 mrad from 10 Hz to 25 kHz (see Fig. 5).

As clearly seen in Fig. 4(c), above the −130 dBm measurement noise, the primary contributions to the phase noise are in the ±1 kHz band around the carrier frequency. The spectral power of the carrier signal at 47 MHz is about 75 dB higher than the white noise. From the power spectral density (PSD) in Fig. 4(c), one can calculate the single sideband phase noise $\mathcal{L}(f)$ (dBc/Hz), which is defined as single sideband power due to phase fluctuations referenced to carrier power. From the PSD in Fig. 4(c), we could estimate the white-noise equivalent phase noise at, e.g., 2.5 kHz, as $\mathcal{L}(2.5\text{ kHz}) = P_n(\text{dBm/Hz}) - P_s(\text{dBm}) = -73$ dBc/Hz, where $P_n = -130$ dBm/Hz is the white noise and $P_s = -57$ dBm is the carrier power at 47 MHz. Here we assume that there is equal contribution of the phase noise and amplitude noise to estimate the phase noise from the power spectral density measured by the RFSA of which input impedance is 50 Ω.

Now, one can calculate the phase noise PSD, $S_\phi(f)$ (rad^2/Hz), from the measured $\mathcal{L}(f)$ (dBc/Hz) and using the relation of $S_\phi(\text{f}) = 2\mathcal{L}(f) = \Delta\Phi_{\rm rms}^2/\text{RB}$, where $\Delta\Phi_{\rm rms}^2$ is the root-mean-square PSD. In this way, we measured the integrated phase noise from $p = 2$ to 25 as shown in Fig. 5(b). In particular, to calculate the integrated phase noise in Fig. 5(b), we measured the high resolution PSD with the RB of 5.1 Hz from 10 Hz to 25 kHz from the carrier frequency of the beat note associated with each pulse picking order p. As an example, Fig. 5(a) shows the high resolution PSD (left vertical axis, blue line) for $p = 25$ at the carrier frequency of 27 MHz and its integrated phase noise is plotted (right vertical axis, red line). As clearly seen in Fig. 5, the phase noise of the down-picked OFC is well preserved from that of the fundamental OFC, i.e., the PSRD presented in Fig. 1 introduces an extra phase noise of 59 ± 6 mrad only across the whole pulse picking order from $p = 2$ to 25. Here experimental uncertainty of 6 mrad is the sample standard deviation. It should be noted that for all values of p, as described in Sec. II, a gating pulse width of 4 ns was used to generate SCWP to drive the pulse-picking AOM in PSRD, except to $p = 2$, 4, 8, and 9, where the gating pulse width was 2 ns, i.e., a half-cycle wave packet was used because it gives better SNR to measure the phase noise in Fig. 5(b).

As can be seen from the representative traces in Figs. 4(c) and 5(a), the major contribution of the phase noise of the down-picked OFC originated from the acoustic noise having its noticeable power spectrum less than 1 kHz, since the two optical paths to measure the phase noise in Fig. 5(a) are not actively stabilized. Other than the acoustic noise, which can be stabilized by using the feed-forward technique [39], we found that there is no phase noise contribution from the PSRD itself since it strictly satisfies the synchronous condition given in Ref. [37] for the pulse-picking process of the OFC using an AOM, which keeps the phase noise stability as well as amplitude stability of the down-picked OFC.

V. CONCLUSION

We demonstrated the PSRD of an OFC with $f_{\rm rep} = 250$ MHz at 530 nm with selectable integer pulse picking order $p = 2$ to 25 by using an AOM driven by phase-synchronized SCWPs as a pulse picker. The presented PSRD shows phase-stable pulse picking feature with the average phase noise of 59 ± 6 mrad from 10 Hz to 25 kHz. In particular, for $p = 25$, the down-picked OFC with $f_{\rm rep} = 10$ MHz and $f_{\rm ceo} = 0$ MHz has the PPTI of 100 ns so that it may provide a way to generate an equiphased single-photon frequency comb by using the StPDC processes and to detect single photons one-by-one in a time-bin resolved manner [33]. In this particular application, low phase noise may provide high temporal resolution in the single-photon counting process, since the train of incoming photons are perfectly localized into time bins separated by 100 ns, which is much longer than the dead time of the SAPD. This may also enable the detection of single-photon interference fringe with high visibility due to the high temporal indistinguishability of the single photons from two different single-photon frequency combs, which is critical in the quantum information processing applications [22,28] as well as in the frequency comb single-photon interferometry in particular [19,33].

ACKNOWLEDGMENTS

This work was supported by NRF-2019R1A2C2009974 and T.H.Y. was supported in part by IBS-R023-D1.

APPENDIX: TEMPORAL AND SPATIAL OVERLAP ISSUES OF THE PSRD

There is a conflicting issue [40] related to the proper value of the beam waist w_0 at the AOM of the PSRD related to the temporal overlap of the pulses of the fundamental OFC with the SCWP as it travels across the focused beam waist and to the spatial overlap between the pulses of the down-picked OFC and those of the undiffracted fundamental OFC. It is required, on the one hand, that only a single optical pulse interacts with the SCWP during its transit across the focused beam waist so that adjacent pulses of the fundamental OFC should not be diffracted into the down-picked OFC (temporal overlap issue). On the other hand, a wide separation angle between the zeroth- and first-order diffracted beams (spatial overlap issue) is necessary for the complete separation of the train of pulses of the down-picked OFC from that of the fundamental OFC after the AOM for further use. In this Appendix the trade-off relation between the temporal and spatial overlap issues is elaborated with reference to our experimental configuration.

1. Temporal overlap

Within the AOM aperture, the transit time $\Delta\tau$ required for the SCWP in Fig. 1 in the main text to traverse across the focused optical beam waist w_0 can be defined as

$$\Delta\tau = 2w_0/v_a, \tag{A1}$$

where w_0 is the radius of the focused Gaussian beam and $v_a = 4200$ m/s is the acoustic wave velocity in the $\mathrm{TeO_2}$ crystal of the AOM used for the PSRD. Thus, to control the transit time $\Delta\tau$ one needs to adjust the Gaussian beam waist w_0 at the beam focus. Therefore, to minimize the temporal overlap of the adjacent pulses with the SCWP at the AOM, the Gaussian beam should be conditioned to have $w_0 < w_0^{\max}$ at the focus inside the AOM. Since the PPTI of the fundamental OFC is $T = 1/f_c = 4$ ns, the maximum beam waist $w_0^{\max}$ can be calculated as $w_0^{\max} = 8.4\ \mu$m from Eq. (A1) and the condition of $\Delta\tau \leqslant T$. It should be noted that w_0 is the beam radius at the focus where the field intensity has decreased to $1/e^2$ of its axial value. Thus, field intensity of the Gaussian beam does not drop to zero outside $2w_0$ but has exponentially decaying tails, resulting in the side peaks (SPs) in Fig. 3(b) at the beam waist $w_0 = 1.5w_0^{\max}$ (see below).

2. Spatial overlap

Now, consider that each pulse of the fundamental OFC interacts with the SCWP and diffracts off into the the positive first-order beam as shown in Fig. 1. It is of interest to isolate the first-order beam completely from the undiffracted one so that the first-order diffracted pulse can be picked off from the zeroth-order pulses for further use. Both the zeroth- and first-order beams have an "edge" defined again by the $1/e^2$ drop of axial field intensity. To avoid the spatial overlap between the zeroth- and first-order beams at the collimation lens L2 after the AOM, the edge-to-edge separation angle θ_s between them needs to be considered. If $\theta_s > 0$, the spatial overlap between them decreases as diffracted beam propagates away from the AOM. However, if $\theta_s < 0$, the first-order becomes increasingly difficult to pick off cleanly as it overlaps with the zeroth-order beam always. The separation angle between the first-order and undiffracted beams is defined as

$$\theta_s = \theta_{0-1} - 2\theta_{\mathrm{div}}, \tag{A2}$$

where $\theta_{0-1} = 2\theta_{\mathrm{B}} = \frac{\lambda f_c}{v_a} \simeq 0.032$ rad is the angle between the zeroth- and first-order diffracted beams and θ_{B} is the Bragg angle, while $\theta_{\mathrm{div}} = \frac{\lambda}{\pi w_0}$ is the divergence angle of the Gaussian beam from the beam waist, which is assumed to be identical for both diffracted beams. If f_2 is the focal length of L2, then the edge-to-edge separation distance d_s between the zeroth- and first-order beams at the position of L2 is given by $d_s = f_2 \tan\theta_s$. Thus, to separate the first-order diffracted beam out of the undiffracted one the condition $\theta_s > 0$, i.e., $\theta_{\mathrm{div}} < \theta_{0-1}/2 = 0.016$ rad, should be met.

If we look at the Eqs. (A1) and (A2) closely, we immediately realize that there is a trade-off relation of the beam waist w_0 at the AOM to make $\Delta\tau$ ($\propto w_0$) smaller to avoid the temporal overlap among adjacent pulses of the fundamental OFC at the AOM versus to make θ_{div} ($\propto 1/w_0$) smaller to avoid the spatial overlap between the first- and zeroth-order diffracted beams for fixed experimental parameters. For example, $\theta_{0-1} = 0.032$ rad is fixed in the present experiment, then the minimum beam waist for fixed $f_c = 250$ MHz may be given as $w_0^{\min} = 2v_a/(\pi f_c) \simeq 10.7\ \mu\text{m} > w_0^{\max} = 8.4\ \mu$m. It turns out that it is impossible to find unique w_0 satisfying the condition of $\theta_{\mathrm{div}} < 0.016$ rad without sacrificing the condition of $\Delta\tau < 4$ ns, i.e., without the temporal overlap in Eq. (A1). Therefore, it is clear that we need to choose the proper value of w_0 (trade-off optimization) that allows minimum temporal overlap to make w_0 slightly larger than $w_0^{\min}$ and reasonable separation distance d_s at the position of L2, e.g., $d_s \simeq 1$ mm, to separate the first-order diffracted beam effectively from the zeroth-order beam with reasonable choice of f_2. Here we note that the Rayleigh range $z_{\mathrm{R}} = n\pi w_0^2/\lambda = 2.2$ mm, where $n = 2.3$ is the refractive index of the AOM at $\lambda = 530$ nm and L is the AOM length, is slightly less than $L/2 = 3$ mm.

3. Trade-off optimization

As discussed above, the trade-off relation depends on the proper selection of w_0. In our approach, w_0 should be sufficiently larger than $w_0^{\max}$ to prevent negative d_s. To do this, we follow the simple procedure as follows. From the measured beam radius of $w_{\text{in}} = 572\ \mu\text{m}$ of the collimated input beam at the focusing lens L1 in Fig. 1, we choose the focal length of L1 as $f_1 = 40$ mm to get $w_0 = 11.8\ \mu\text{m} > w_0^{\text{max}}$. Then we take $d_s = 1$ mm as a target value at the L2 to select f_2 so that there is enough edge-to-edge separation between first- and zeroth-order diffracted beams at L2. Based on these considerations, we choose $f_2 = 300$ mm for the effective pulse picking up to the input power of $P_{\text{in}} = 204$ mW as shown in Fig. 2. Experimentally, we measured $w_0 = 12.6\ \mu\text{m}$ using a beam profiler (CCD-2302-RT, Cinogy Technologies) close to the calculated value of $11.8\ \mu\text{m}$. With these optimum trade-off parameters, there is nonzero temporal overlaps from the adjacent pulses having 16.4% residual powers compared to the main power of the picked pulses at the total power of 3.1 mW of the down-picked OFC at $P_{\text{in}} = 204$ mW. In the AOM aperture, the phase of the SCWP is adjusted such that the optical pulse interacts with the center of the wave packet. In this way both preceding and succeeding satellite pulses have the same powers as can be seen in Fig. 3(b). There is an 8-ns time separation between three successive optical pulses within the AOM during the passage of the SWCP so that one may anticipate that $\Delta\tau \leqslant 6$ ns is short enough for clean temporal pickup without satellite peaks. However, this is not the case because the SCWP still interacts with the tail of the Gaussian beam beyond the $1/e^2$ drop and thus diffracts adjacent pulses that are visible as the side peaks in Fig. 3(b) of the main text. Aberrations that can reduce beam quality from the ideal Gaussian beam may further impede side peak suppression but these were not considered in our theoretical model. The AOM used in this demonstration is made of tellurium oxide that has the speed of sound $v_a = 4200$ m/s. Superior side peak suppression is anticipated either by using a different AOM material that has the speed of sound faster than that of TeO_2, i.e., $v_a > 4200$ m/s (e.g., crystal quartz), using a fundamental OFC with lower repetition rate, or by driving the AOM with the higher carrier frequency, i.e., $f_c \gg f_{\text{rep}} = 250$ MHz.

[1] J. L. Hall, Rev. Mod. Phys. **78**, 1279 (2006).

[2] T. W. Hänsch, Rev. Mod. Phys. **78**, 1297 (2006).

[3] T. M. Fortier and E. Baumann, Commun. Phys. **2**, 153 (2019).

[4] T. Rosenband, D. B. Hume, P. O. Schmidt, C. W. Chou, A. Brusch, L. Lorini, W. H. Oskay, R. E. Drullinger, T. M. Fortier, J. E. Stalnaker, and S. A. Diddams, Science **319**, 808 (2008).

[5] N. Picqué and T. W. Hänsch, Nat. Photon. **13**, 146 (2019).

[6] S. A. Diddams, L. Hollberg, and V. Mbele, Nature (London) **445**, 627 (2007).

[7] J. Lee, Y.-J. Kim, K. Lee, S. Lee, and S.-W. Kim, Nat. Photon. **4**, 716 (2010).

[8] M. G. Suh and K. J. Vahala, Science **359**, 884 (2018).

[9] M. Kues, C. Reimer, J. M. Lukens, W. J. Munro, A. M. Weiner, D. J. Moss, and R. Morandotti, Nat. Photon. **13**, 170 (2019).

[10] J.-I. Yoshikawa, S. Yokoyama, T. Kaji, C. Sornphiphatphong, Y. Shiozawa, K. Makino, and A. Furusawa, APL Photonics **1**, 060801 (2016).

[11] C. Reimer, M. Kues, P. Roztocki, B. Wetzel, F. Grazioso, B. E. Little, S. T. Chu, T. Johnston, Y. Bromberg, L. Caspani, D. J. Moss, and R. Morandotti, Science **351**, 1176 (2016).

[12] W. N. Plick, F. Arzani, N. Treps, E. Diamanti, and D. Markham, Phys. Rev. A **98**, 062101 (2018).

[13] H.-H. Lu, A. M. Weiner, P. Lougovski, and J. M. Lukens, IEEE Photon. Technol. Lett. **31**, 1858 (2019).

[14] C. Cui, K. P. Seshadreesan, S. Guha, and L. Fan, Phys. Rev. Lett. **124**, 190502 (2020).

[15] Y.-S. Ra, A. Dufour, M. Walschaers, C. Jacquard, T. Michel, C. Fabre, and N. Treps, Nat. Phys. **16**, 141 (2020).

[16] O. Pfister, J. Phys. B: At. Mol. Opt. Phys. **53**, 012001 (2020).

[17] V. Giovannetti, S. Lloyd, and L. Maccone, Nat. Photon. **5**, 222 (2011).

[18] D. A. Kalashnikov, A. V. Paterova, S. P. Kulik, and L. A. Krivitsky, Nat. Photon. **10**, 98 (2016).

[19] S. K. Lee, T. H. Yoon, and M. Cho, Opt. Express **27**, 14853 (2019).

[20] G. B. Lemos, V. Borish, G. D. Cole, S. Ramelow, R. Lapkiewicz, and A. Zeilinger, Nature (London) **512**, 409 (2014).

[21] Y. J. Lu, R. L. Campbell, and Z. Y. Ou, Phys. Rev. Lett. **91**, 163602 (2003).

[22] Z. Xie, T. Zhong, S. Shrestha, X. A. Xu, J. Liang, Y.-X. Gong, J. C. Bienfang, A. Restelli, J. H. Shapiro, F. N. C. Wong, and C. W. Wong, Nat. Photon. **9**, 536 (2015).

[23] P. Imany, O. D. Odele, J. A. Jaramillo-Villegas, D. E. Leaird, and A. M. Weiner, Phys. Rev. A **97**, 013813 (2018).

[24] R. Ikuta, R. Tani, M. Ishizaki, S. Miki, M. Yabuno, H. Terai, N. Imoto, and T. Yamamoto, Phys. Rev. Lett. **123**, 193603 (2019).

[25] P. Chen, X. Guo, C. Shu, M. M. T. Loy, and S. Du, Optica **2**, 505 (2015).

[26] J. Park, T. Jeong, H. Kim, and H. S. Moon, Phys. Rev. Lett. **121**, 263601 (2018).

[27] C. Wang, C.-H. Lee, Y. Kim, and Y.-H. Kim, Opt. Lett. **45**, 1802 (2020).

[28] O. Alibart, J. Fulconis, G. K. L. Wong, S. G. Murdoch, W. J. Wadsworth, and J. G. Rarity, New J. Phys. **8**, 67 (2006).

[29] J. A. Jaramillo-Villegas, P. Imany, O. D. Odele, D. E. Leaird, Z.-Y. Ou, M. Qi, and A. M. Weiner, Optica **4**, 655 (2017).

[30] Z. Y. Ou, L. J. Wang, X. Y. Zou, and L. Mandel, Phys. Rev. A **41**, 1597 (1990).

[31] L. Wang, X. Zou, and L. Mandel, J. Opt. Soc. Am. B **8**, 978 (1991).

[32] A. Heuer, R. Menzel, and P. W. Milonni, Phys. Rev. Lett. **114**, 053601 (2015).

[33] S. K. Lee, N. S. Han, T. H. Yoon, and M. Cho, Commun. Phys. **1**, 51 (2018).

[34] S. K. Lee, T. H. Yoon, and M. Cho, Phys. Rev. Appl. **14**, 014045 (2020).

[35] S. Deng, D. Gordon, and A. P. Morrison, IEEE Photon. Technol. Lett. **28**, 99 (2016).

[36] F. Yuan, X.-L. Lu, L. Jing, Y.-X. Yang, F.-L. Kong, S.-J. Deng, C. Guo, and H.-Z. Song, in *Proceedings of the IEEE 4th Optoelectronics Global Conference (OGC), Shenzhen, China* (IEEE, Piscataway, NJ, 2019), pp. 85–88.

[37] O. de Vries, T. Saule, M. Plötner, F. Lücking, T. Eidam, A. Hoffmann, A. Klenke, S. Hädrich, J. Limpert, S. Holzberger, T. Schreiber, R. Eberhardt, I. Pupeza, and A. Tünnermann, Opt. Express **23**, 19586 (2015).

[38] T. Saule, S. Holzberger, O. De Vries, M. Plötner, J. Limpert, A. Tünnermann, and I. Pupeza, Appl. Phys. B **123**, 17 (2017).

[39] Z. Chen, M. Yan, T. W. Hänsch, and N. Picqué, Nat. Commun. **9**, 3035 (2018).

[40] J. R. Boyd, E. H. Young, and S. K. Yao, Opt. Eng. **16**, 165452 (1977).